

Beating Rayleigh’s Curse by Imaging Using Phase Information

Weng-Kian Tham,^{1,2*} Hugo Ferretti,^{1,2*} Aephraim M. Steinberg^{1,2}

¹Centre for Quantum Information and Quantum Control and Institute for Optical Sciences,

Department of Physics, University of Toronto,

60 St. George St, Toronto, Ontario, Canada, M5S 1A7

²Canadian Institute For Advanced Research,

180 Dundas St. W., Toronto, Ontario, Canada, M5G 1Z8

* These authors contributed equally to this work.

Any imaging device such as a microscope or telescope has a resolution limit, a minimum separation it can resolve between two objects or sources; this limit is typically defined by “Rayleigh’s criterion” [1], although in recent years there have been a number of high-profile techniques demonstrating that Rayleigh’s limit can be surpassed under particular sets of conditions [2, 3, 4]. Quantum information and quantum metrology have given us new ways to approach measurement [5, 6, 7, 8, 9]; a new proposal inspired by these ideas [10] has now re-examined the problem of trying to estimate the separation between two poorly resolved point sources. The “Fisher information” [11] provides the inverse of the Crámer-Rao bound, the lowest variance achievable for an unbiased estimator. For a given imaging system and a fixed number of collected photons, Tsang, Nair and Lu observed that the Fisher information carried by the *intensity* of the light in the image-plane (the only information available to tradi-

tional techniques, including previous super-resolution approaches) falls to zero as the separation between the sources decreases; this is known as “Rayleigh’s Curse.” On the other hand, when they calculated the quantum Fisher information [12, 13] of the full electromagnetic field (including amplitude *and* phase information), they found it remains constant. In other words, there is infinitely more information available about the separation of the sources in the phase of the field than in the intensity alone. Here we implement a proof-of-principle system which makes use of the phase information, and demonstrate a greatly improved ability to estimate the distance between a pair of closely-separated sources, and immunity to Rayleigh’s curse.

As an electromagnetic wave, light is characterized by both an amplitude and a phase. Traditional imaging systems use lenses or mirrors to refocus this wave and project an image of the source onto a screen or camera, where the intensity (or rate of photon arrivals) is recorded at each position. (We refer to all such techniques as “image-plane counting” or IPC.) Although the phase of the wave at the position of the optics plays a central role during the focusing, any information about the phase *in the image plane* is discarded. When light passes through finite-sized optical elements, diffraction smears out the spatial distribution of photons so that point-sources map (via the point-spread-function or PSF) onto finite-sized spots at the image-plane. Thus, our ability to resolve the point-sources is inhibited when their separation in the image-plane, δ , is comparable to or less than the width σ of the PSF.

The typical response to diffraction limits has been to build larger (or higher numerical-aperture) optics, thereby making the PSF sharper/narrower. In recent years, techniques have been developed in specific cases that address these limits in more novel ways [2, 3, 4, 14, 15, 16, 17, 18, 19, 20]. Despite their success, these techniques require careful control of the source of illumination, which is not always possible in every imaging application (e.g. astronomy). In

order to beat the diffraction limit for *fixed, mutually incoherent* sources, a paradigm shift arising from the realisation that there is a huge amount of information available in the phase discarded by IPC may prove revolutionary.

45 It was shown in [10] that whereas in IPC the Fisher Information, I_f , vanishes quadratically with the separation δ between two equal-intensity incoherent point sources of light, it remains undiminished when the full electromagnetic field is considered. Now I_f is related to the performance of a statistical estimator by :

$$\text{Var}(\delta_{est}) \geq \frac{1}{I_f} \left(1 + \frac{\partial(\text{bias})}{\partial \delta_{actual}} \right) \quad (1)$$

50 where δ_{est} is some estimator of δ_{actual} and $\text{bias} \equiv \langle \delta_{est} \rangle - \delta_{actual}$. The vanishing of I_f as $\delta \rightarrow 0$ suggests that for closely separated sources, the variance in an IPC-based estimate of δ is cursed to blow up. Its independence of δ for the full field, on the other hand, immediately leads to the idea that this divergence can be averted by using phase as well as intensity information.

One natural way to do this would be to use SPAtial mode DEMultiplexing (SPADE)[10, 21], in which incoming light is decomposed into its Hermite-Gauss (HG) components and the 55 amplitude of each is measured. It can be shown that the full set of HG amplitudes contains the same I_f as the full EM field. A reduced version called binary SPADE prescribes discriminating only between the TEM_{00} mode and the sum of all other modes. For small δ , only one other mode acquires significant amplitude in any case, so the I_f available to binary SPADE becomes essentially equal to the full Fisher information. The method can be understood as follows: 60 the projection always succeeds ($P_{00} = |\langle \psi | TEM_{00} \rangle|^2 = 1$) when the two point-sources are overlapped ($\delta = 0$), but has a failure probability $1 - P_{00}$ which grows quadratically with δ [22]. Knowing the TEM_{00} component as a proportion of all HG amplitudes (i.e. P_{00} and $1 - P_{00}$) allows one to deduce δ .

Experimentally however, merely capturing the TEM_{00} component (say, by coupling into

65 a single mode fiber) without a normalization factor (which allows us to deduce $1 - P_{00}$) provides no advantage over IPC. Practically speaking, the crucial information comes from a projection onto some mode *orthogonal* to TEM_{00} in order to estimate $1 - P_{00}$. While a mode such as TEM_{10} would contain all the information (for a separation in the x-direction in that example), the same scaling can be obtained by projecting onto any spatially antisymmetric field mode. As a proof-of-principle, we have designed and implemented an experimentally convenient method, SPLICE (Super-resolved Position Localisation by Inversion of Coherence along an Edge), which instead carries out one technically straightforward projection. Consider the mode function $\psi_{\perp}(x, y) = \exp\left(-\frac{x^2+y^2}{4\sigma^2}\right) \text{sign}(x)$, constructed such that its inner product with TEM_{00} vanishes. The probability that such a projection succeeds is:

$$P_{\perp} = \frac{1}{2} \left(|\langle \psi_1 | \psi_{\perp} \rangle|^2 + |\langle \psi_2 | \psi_{\perp} \rangle|^2 \right) = e^{-2\Delta} \text{erf}^2 \sqrt{\Delta} \quad (2)$$

75 where $\Delta = \delta^2/32\sigma^2$, and δ is the separation between point sources on the image plane, and $\psi_{1/2}$ is the field from each source.

The per photon Fisher information can be written as

$$I_f = \frac{\left(e^{-\Delta} \sqrt{\pi \Delta} \text{erf} \sqrt{\Delta} - e^{-2\Delta} \right)^2}{2\pi\sigma^2} + \frac{\left(e^{-\Delta} \sqrt{\pi \Delta} \text{erf}^2(\sqrt{\Delta}) - e^{-2\Delta} \text{erf} \sqrt{\Delta} \right)^2}{2\pi\sigma^2 \left(e^{2\Delta} - \text{erf}^2 \sqrt{\Delta} \right)} \quad (3)$$

where the first term comes from P_{\perp} and the second from $1 - P_{\perp}$. Crucially, as $\Delta \rightarrow 0$, $1 - P_{\perp}$ vanishes, meaning that an experimentally simple scheme for projecting only onto ψ_{\perp} does as well as a more complicated scheme which could measure multiple projections simultaneously. In (*Fig. 1.*), we plotted the Fisher information for SPLICE in comparison with other methods. It is easy to see that it remains constant as $\delta \rightarrow 0$, evading Rayleigh's curse, and extracting nearly 2/3 of the total information available to full SPADE using an experimentally simple technique. More sophisticated methods relying on waveguides or cavities could be designed to approach 100% of the total I_f .

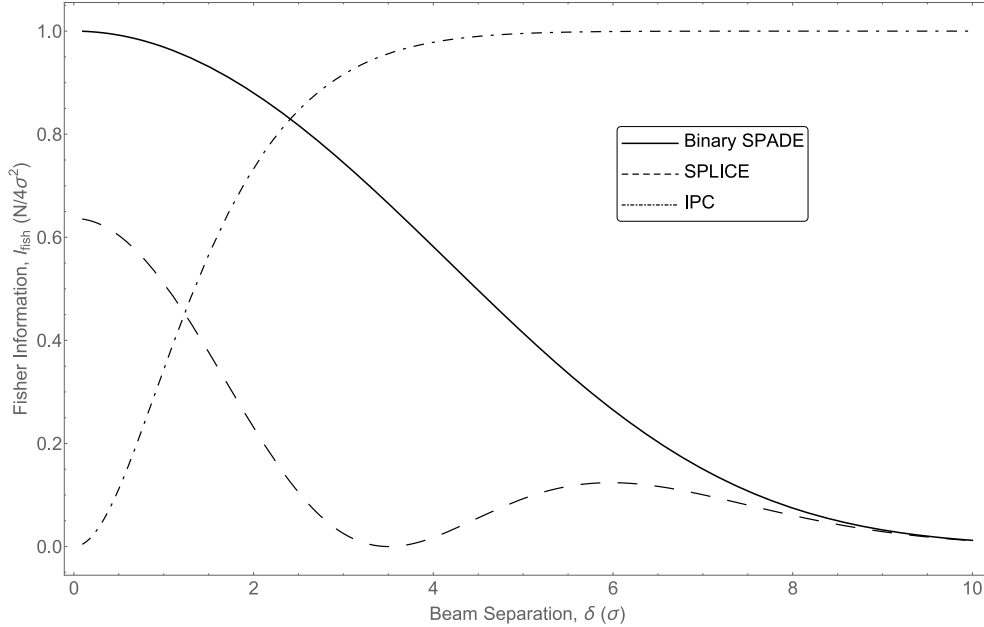


Figure 1: **Fisher information for SPLICE, binary SPADE, and IPC** Theory plot of Fisher information for various methods vs beam separation δ , normalized to units of $N/4\sigma^2$ and σ respectively.

In order to experimentally demonstrate improved performance over IPC, we used two mutually incoherent collimated TEM_{00} Gaussian beams in place of distant point sources and an imaging optical setup. The beams were directed through a Sagnac-like beam displacer shown in (Fig. 2.). By moving a mirror on a motorized translation stage as shown, we precisely control the separation δ between the otherwise parallel beams. The separation is induced symmetrically, such that the geometrical centroid (x_0, y_0) remains static.

Our light source is an 805-nm heralded single-photon source which relies on type-I spontaneous parametric down-conversion (SPDC) in a 2mm-thick BBO crystal. The crystal is pumped by 402.5 nm light obtained from a frequency-doubled 100-fs Ti:Sapph laser. One photon from the SPDC pair is used to herald the presence of a signal photon and as a means of rejecting spurious background light (our accidental coincidences average 2 ± 1 counts/sec). In order to emulate two point sources, the other photon is split at a 50/50 fiber-splitter and out-coupled to free-space.

The two resulting beams are incoherent; they have splitter-to-coupler distances that differ by 5cm whereas the SPDC photons are filtered to $\Delta\lambda = 3nm$ (i.e. coherence length $\approx 10\mu m$).
 100 ND filters were used to reduce the intensity imbalance between the beams to $\approx (3 \pm 3) \%$.

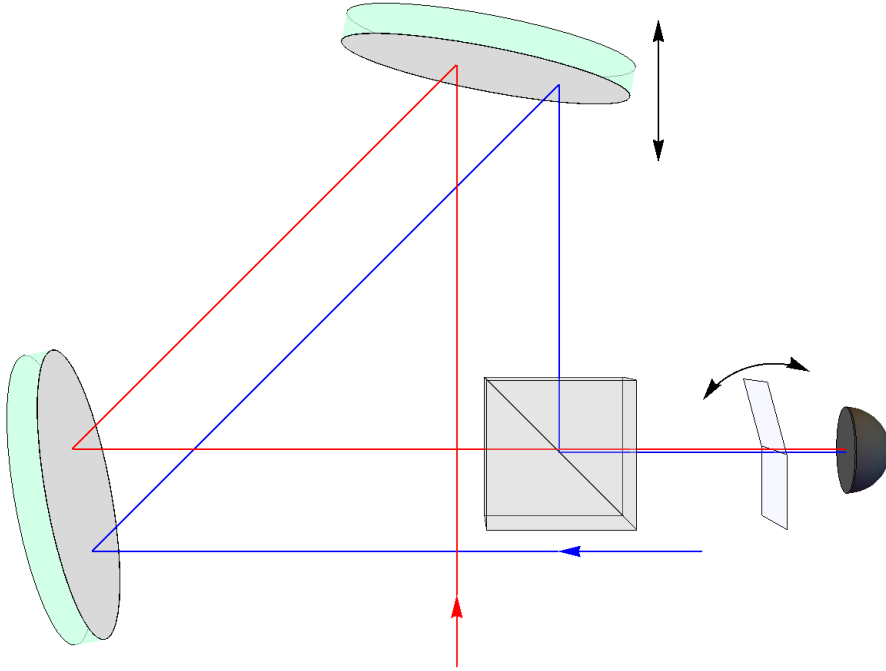


Figure 2: **Cartoon of experiment.** Shown is the apparatus for generating the symmetrically displaced pair of sources, and the phase-shifter used for implementing SPLICE.

At zero separation, the beams are overlapped and are both coupled into single-mode TEM_{00} fiber (coupling efficiencies are 90% and 85% respectively). Collimation of the beams is such that their waists are closely matched immediately before the fiber coupler ($\sigma = 614 \pm 4\mu m$ and $594 \pm 10\mu m$) in order to emulate Gaussian point spread functions of distant sources. The pro-
 105 jection onto ψ_{\perp} is achieved by inserting a phase plate immediately in front of the coupler such that when $\delta = 0$, a semi-circular cross-section of the beams undergoes a π -phase shift whereas the other half experiences none. The phase plate consists of a transparent glass microscope slide with a sharp rectangular edge mounted on a translation and rotation stage and positioned/rotated

to minimize coupling into an otherwise well-aligned coupler. Typical visibility is $\geq 99\%$.

110 To compare the performance of our method with a more traditional imaging setup, we replaced the phase plate with a $200\mu\text{m}$ slit that served as the image plane, coupling all the light transmitted through the slit into a multimode fibre. Scanning the slit, we were able to perform one-dimensional IPC.

With SPLICE, the separation of the incoherent beams was scanned, with the detectors counting for 1 second at each step. Two sets of these “phase-plate” scans were performed, one at 115 coarse intervals of δ (spanning -1.96mm to $+1.94\text{mm}$, in steps of 0.1mm) and another at finer intervals ($-0.56\text{mm} \leq \delta \leq +0.44\text{mm}$ in steps of 0.04mm). Data from nine repetitions of the coarse scan and fifteen of the fine scan were recorded.

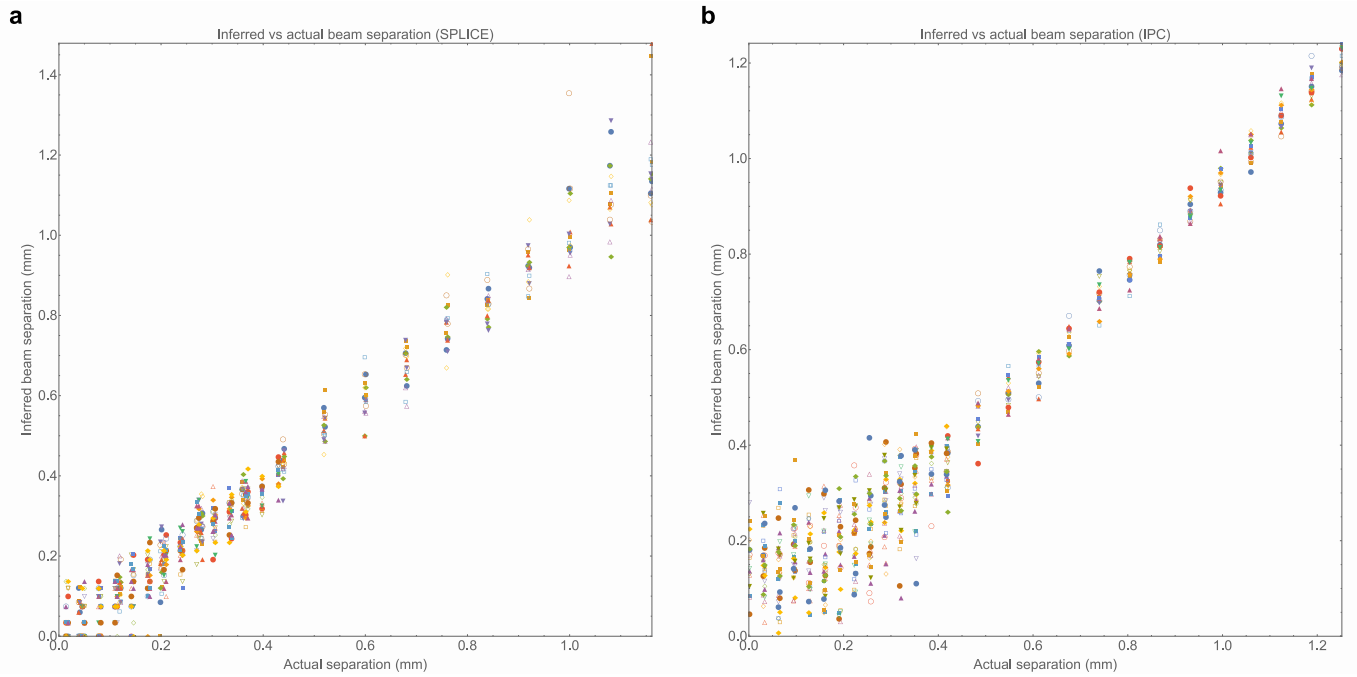


Figure 3: **Inferred separation vs known actual separation** for a) SPLICE (from “lookup” on calibration curve) and b) IPC.

Whereas the ideal functional form for the resulting counts vs separation δ is proportional to

120 equation 2, we add a constant γ to account for residual background counts:

$$\text{SPLICE counts} = \alpha \exp\left(-\frac{\delta^2}{16\sigma^2}\right) \text{erf}^2\left(\frac{\delta}{4\sqrt{2}\sigma}\right) + \gamma \quad (4)$$

A calibration curve was obtained from a least squares fit of this function to data from a longer run (2 sec count time instead of 1 sec for each δ), from which the beam waist σ , position offset for the motorized translation stage, and count offset γ due to accidentals/background were deduced. This step might be thought of as being analogous to characterizing one's imaging
 125 optics before use. One might then use the curve as a “lookup table” from which δ is estimated from count rates. We performed such a lookup with the remainder of our data. The *estimated* δ is plotted versus their *actual* values (as reported by motorized translation stage controllers) in (Fig. 3a.).

The traditional image plane counting data were acquired using the configuration described
 130 above, scanning the 200 μm slit between -1mm and $+1\text{mm}$ of the centroid of the two beams, counting for 4 seconds at each step. Again, we repeated this for various separations δ and in turn repeated the whole scan several times. As before, a set of coarse scans ($-0.04\text{mm} \leq \delta \leq 1.56\text{mm}$ in steps of 0.08mm , 16 repetitions) and a set of fine scans ($-0.52\text{mm} \leq \delta \leq 0.44\text{mm}$ in steps of 0.04mm , 17 repetitions) were performed Estimation of δ in this IPC comparison was
 135 done by least-squares fitting the resulting image plane intensity profile to

$$\text{IPC counts} = \alpha [\text{exp}_- + \text{exp}_+ + \gamma] \quad (5)$$

where $\text{exp}_\pm = \exp\left[-(x \pm \delta/2)^2 / 2\sigma^2\right]$. Again, a calibration waist σ and background γ were obtained beforehand, leaving the scale α and separation δ as the only fitting parameters. In practice, the fitting procedure used to fit IPC data for small δ was different from the one used to treat data for large δ . For the latter, we simply used built-in numerical algorithms in Mathematica and NumPy. For small δ 's however, the routines exhibited convergence and stability issues,
 140 forcing us to Taylor expand equation 5 to 2nd order in δ and manually invert the resulting 2×2

design matrix. The resulting estimated separations are plotted against actual separations in (Fig. 3b.). As is immediately apparent, for separations below about 0.25mm (approximately 0.4σ), the spread of the IPC data begins to grow, while that of the SPLICE data remains essentially constant.

145

Two key metrics for the performance of either method are the standard deviation or SD (i.e. “spread”) and root-mean-square error (RMSE) of the estimated beam separation. The SD measures the *precision* of a dataset but not necessarily its accuracy, while the RMSE is sensitive to the accuracy since it quantifies the error relative to a known actual value and not simply the reported result. In (Fig. 4. and Fig. 5.), SD and RMSE are plotted versus known actual separations.

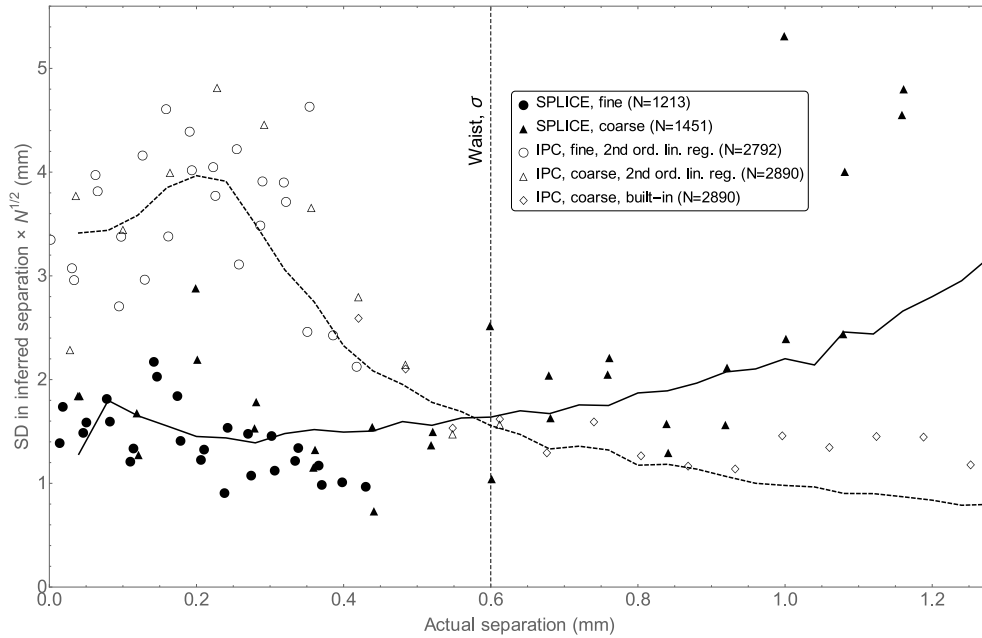


Figure 4: **Uncertainty comparison between SPLICE and IPC.** Standard Deviation (SD) in the estimated separation plotted as a function of actual separation for both IPC and SPLICE. The computed SD for each dataset is *multiplied* by photon number (\sqrt{N}). Overlaid lines are the corresponding Monte Carlo simulations. Note that two methods were used in the fitting of IPC data to equation 5; for small δ ($< 0.65mm$), equation 5 was expanded to 2nd order and linear regression was performed whereas for large δ ($> 0.4mm$), a nonlinear fitting routine built into Mathematica was used.

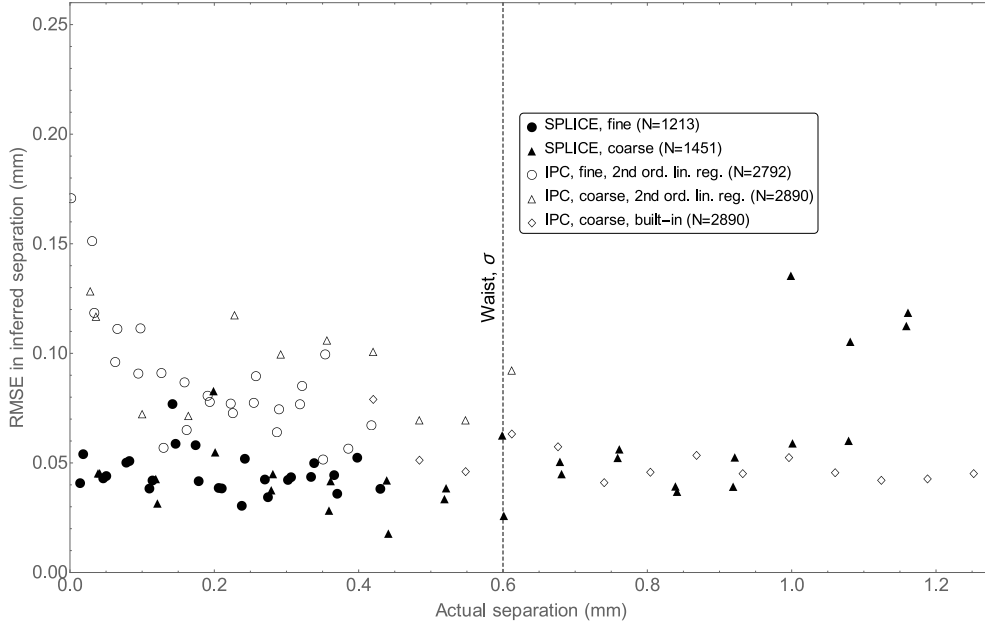


Figure 5: **Un-normalized Root Mean-Square Error (RMSE)** in the estimated separation vs actual separation for both IPC and SPLICE. Unlike SD, the RMSE allows us to gauge absolute error relative to the known actual value of the parameter being estimated so that biases are accounted for. Note that two methods were used in the fitting of IPC data to equation 5; for small δ ($< 0.65mm$), equation 5 was expanded to 2nd order and linear regression was performed whereas for large δ ($> 0.4mm$), a nonlinear fitting routine built into Mathematica was used.

In order to ensure a reasonably even-footed comparison between IPC and SPLICE, the spreads in inferred separation plotted in (Fig. 4.) are scaled by \sqrt{N} (where N is the photon number that comprises a measurement) to reflect the fact that noise in photon counts at our detector is Poissonian. For IPC, N is simply the total photons that comprise an “image” on the image plane, which in our case is actually a set of photon counts, one at each position of the 200 μ m slit. For SPLICE, during a calibration run, we estimate N by counting at our detector over a 1 second window while both beams are centered (i.e. $\delta = 0$) on the coupler into TEM_{00} fiber with the *phase-plate removed*. Since our source intensity is stable, this gives us an *estimate* of the number of incident photons for subsequent measurements when $\delta \neq 0$.

The RMSE plotted in (Fig. 5.) is *not* similarly normalized because in addition to possible

systematics, the inferred separation is biased relative to the actual separation when δ is small. A priori, there is no reason to suspect either bias or systematics to scale as \sqrt{N} . Despite *not* normalizing and despite using approximately twice as many photons, the IPC method performs
165 noticeably *worse* than SPLICE when $\delta < 0.6mm$.

The attentive reader will note that while the spread is greater for IPC, it does not diverge as $\delta \rightarrow 0$. In fact, it would be implausible for the uncertainty on δ to ever exceed σ . The apparent discrepancy with the vanishing of the Fisher information can be understood by recognizing that (as is clear from inspection of (*Fig. 1.*) at small δ) the practically implemented IPC estimator is
170 not unbiased. To better understand the bounds on the advantage that one can expect of SPLICE over IPC, we return to equation 1. Clearly, one needs to know the bias to evaluate the RHS. For SPLICE, the only potential source of bias is the lookup procedure. If, for example, a less-than-perfect visibility results in a calibration curve that does not vanish at $\delta = 0$, then one might obtain “unphysical” datapoints that fall *under* the minima of the calibration curve,
175 thereby resulting in a bias when a lookup is attempted. In our case, this is negligible since our visibility exceeds 99%. The CRLB is therefore just the reciprocal of I_f , implying a $1/\sqrt{N}$ scaling in the spread of δ_{est} .

With IPC, the least-squares estimate of δ is heavily biased at small δ . An intuitive way to understand this is to note that since the problem being addressed is the resolving of two *equal*
180 *intensity* sources, the $+\delta$ and $-\delta$ cases are physically indistinguishable. This is equivalent to saying that the power series expansion of equation 5 consists only of *even* powers of δ . Given no additional information about the sign of δ , we restrict δ to be positive without loss of generality. But in doing so, as long as spread in the estimated δ is non-zero, the *mean* estimated δ is never zero. (*Fig. 6.*) shows a plot of mean inferred δ (averaged across all our datasets) vs actual δ .
185 Overlaid is a theory curve for IPC, which takes into account an expected bias at small δ .

In [23], we present theory showing that the bias term for IPC falls to -1 sufficiently quickly

that the RHS of inequality 1 tends to a finite value as $\delta \rightarrow 0$. That finite value is shown to scale as $N^{-1/4}$, which is in stark contrast to the behaviour of the spread at large δ (for IPC) as well as for SPLICE (at all δ), where a Poissonian scaling of $N^{-1/2}$ is obeyed. This scaling
190 is further substantiated with Monte-Carlo simulations shown in a figure in [23]. Thus while SPLICE does not offer an *infinite* advantage over IPC as a naive analysis might have us believe, it *does* nevertheless offer a substantial improvement in the absolute error and the scaling with photon number, while simultaneously eliminating the problem of bias.

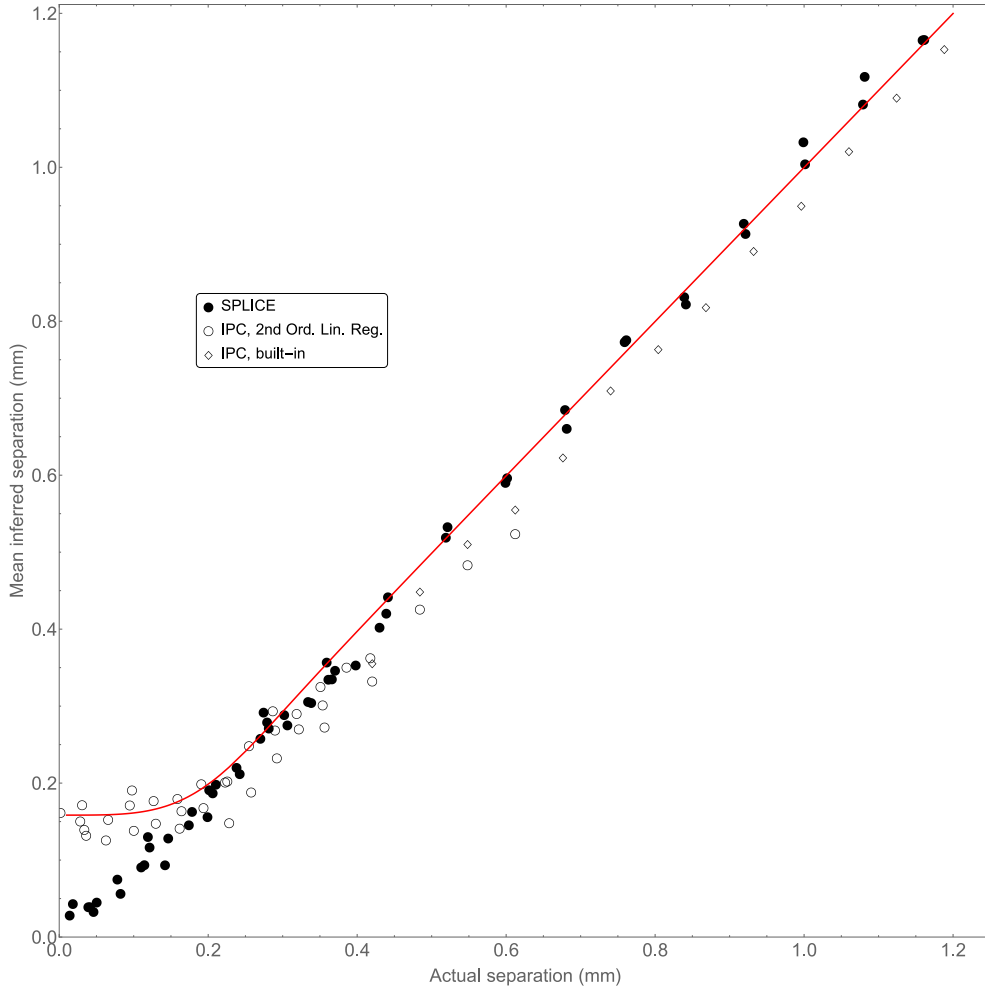


Figure 6: **Averaged measured separations.** Mean estimated δ for IPC and SPLICE plotted against known actual δ . Two methods were used in the fitting of IPC data to equation 5; for small δ ($< 0.65mm$), equation 5 was expanded to 2nd order and linear regression was performed whereas for large δ ($> 0.4mm$), a nonlinear fitting routine built into Mathematica was used.

In summary, we have developed and demonstrated a simple technique that surpasses tradi-
 195 tional imaging in its ability to resolve two closely spaced point-sources. Furthermore, unlike
 existing superresolution methods, ours requires no exotic illumination with particular coher-
 ence/quantum properties and is applicable to classical incoherent sources. Crucially, as a proof-
 of-principle, this technique highlights the importance of realising that diffraction-imposed reso-
 lution limits are *not* a fundamental constraint but, instead, the consequence of traditional imag-

200 ing techniques discarding the phase information present in the light. We expect that this and other related techniques that do not discard the phase information will be developed in the future for a broad range of imaging applications.

Note: While preparing this manuscript, we came to realise that similar work was being pursued by Yang et al [24] and Sheng et al [25].

205 **References and Notes**

- [1] Lord Rayleigh. XXXI. Investigations in optics, with special reference to the spectroscope. *Philosophical Magazine Series 5* **8**, 261–274 (1879). URL <http://dx.doi.org/10.1080/14786447908639684>.
- [2] Hell, S. W. & Wichmann, J. Breaking the diffraction resolution limit by stimulated emission: stimulated-emission-depletion fluorescence microscopy. *Optics letters* **19**, 780–782 (1994).
- [3] Betzig, E. *et al.* Imaging intracellular fluorescent proteins at nanometer resolution. *Science* **313**, 1642–1645 (2006).
- [4] Hess, S. T., Girirajan, T. P. & Mason, M. D. Ultra-high resolution imaging by fluorescence photoactivation localization microscopy. *Biophysical journal* **91**, 4258–4272 (2006).
- [5] Giovannetti, V., Lloyd, S. & Maccone, L. Quantum-enhanced measurements: beating the standard quantum limit. *Science* **306**, 1330–1336 (2004).
- [6] Giovannetti, V., Lloyd, S. & Maccone, L. Advances in quantum metrology. *Nature Photonics* **5**, 222–229 (2011).
- 220 [7] Mitchell, M. W., Lundeen, J. S. & Steinberg, A. M. Super-resolving phase measurements with a multiphoton entangled state. *Nature* **429**, 161–164 (2004).

- [8] Walther, P. *et al.* De broglie wavelength of a non-local four-photon state. *Nature* **429**, 158–161 (2004).
- [9] Nagata, T., Okamoto, R., O’Brien, J. L., Sasaki, K. & Takeuchi, S. Beating the standard
225 quantum limit with four-entangled photons. *Science* **316**, 726–729 (2007).
- [10] Tsang, M., Nair, R. & Lu, X. Quantum theory of superresolution for two incoherent optical point sources. *arXiv preprint arXiv:1511.00552* (2015).
- [11] Casella, G. & Berger, R. L. *Statistical inference*, vol. 2 (Duxbury Pacific Grove, CA, 2002).
- 230 [12] Helstrom, C. W. Quantum detection and estimation theory. *Journal of Statistical Physics* **1**, 231–252 (1969).
- [13] Petz, D. & Ghinea, C. Introduction to quantum fisher information. *Quantum Probability and Related Topics* **1**, 261–281 (2011).
- [14] Hemmer, P. R. & Zapata, T. The universal scaling laws that determine the achievable
235 resolution in different schemes for super-resolution imaging. *Journal of Optics* **14**, 083002 (2012).
- [15] Giovannetti, V., Lloyd, S., Maccone, L. & Shapiro, J. H. Sub-rayleigh-diffraction-bound quantum imaging. *Physical Review A* **79**, 013827 (2009).
- [16] Tsang, M. Quantum imaging beyond the diffraction limit by optical centroid measure-
240 ments. *Physical review letters* **102**, 253601 (2009).
- [17] Shin, H., Chan, K. W. C., Chang, H. J. & Boyd, R. W. Quantum spatial superresolution by optical centroid measurements. *Phys. Rev. Lett.* **107**, 083603 (2011).

- [18] Rozema, L. A. *et al.* Scalable spatial superresolution using entangled photons. *Phys. Rev. Lett.* **112**, 223602 (2014).
- 245 [19] Tamburini, F., Anzolin, G., Umbriaco, G., Bianchini, A. & Barbieri, C. Overcoming the rayleigh criterion limit with optical vortices. *Phys. Rev. Lett.* **97**, 163903 (2006).
- [20] Schwartz, O. *et al.* Superresolution microscopy with quantum emitters. *Nano letters* **13**, 5832–5836 (2013).
- [21] Richardson, D., Fini, J. & Nelson, L. Space-division multiplexing in optical fibres. *Nature*
250 *Photonics* **7**, 354–362 (2013).
- [22] For circular apertures, the point spread functions are Airy rings. In practice, these are often well-approximated by Gaussians. Within this approximation, two overlapped point-sources map simply to a single Gaussian.
- [23] Supplementary material and extended data are available online.
- 255 [24] Yang, F., Taschilina, A., Moiseev, E. S., Simon, C. & Lvovsky, A. I. Far-field linear optical superresolution via heterodyne detection in a higher-order local oscillator mode. *ArXiv e-prints* (2016). 1606.02662.
- [25] Sheng, T. Z., Durak, K. & Ling, A. Fault-tolerant and finite-error localization for point emitters within the diffraction limit. *arXiv preprint arXiv:1605.07297* (2016).

260 **Acknowledgment**

This work was funded by NSERC, CIFAR, and Northrop-Grumman Aerospace Systems. We would like to thank Mankei Tsang for useful discussions and the Facebook post which led to this collaboration.

Author Contribution

²⁶⁵ W.K.T. and H.F. jointly conducted theoretical analysis, designed and performed the experiment, and analyzed data. A.M.S. conceived of the SPLICE scheme, guided its experimental implementation, and oversaw the research project. All authors contributed to the writing of this article.

Competing Interest

²⁷⁰ We declare no competing financial interests.

Correspondence

Correspondence and material requests should be addressed to H. F. (hferrett@physics.utoronto.ca).

Extended Data

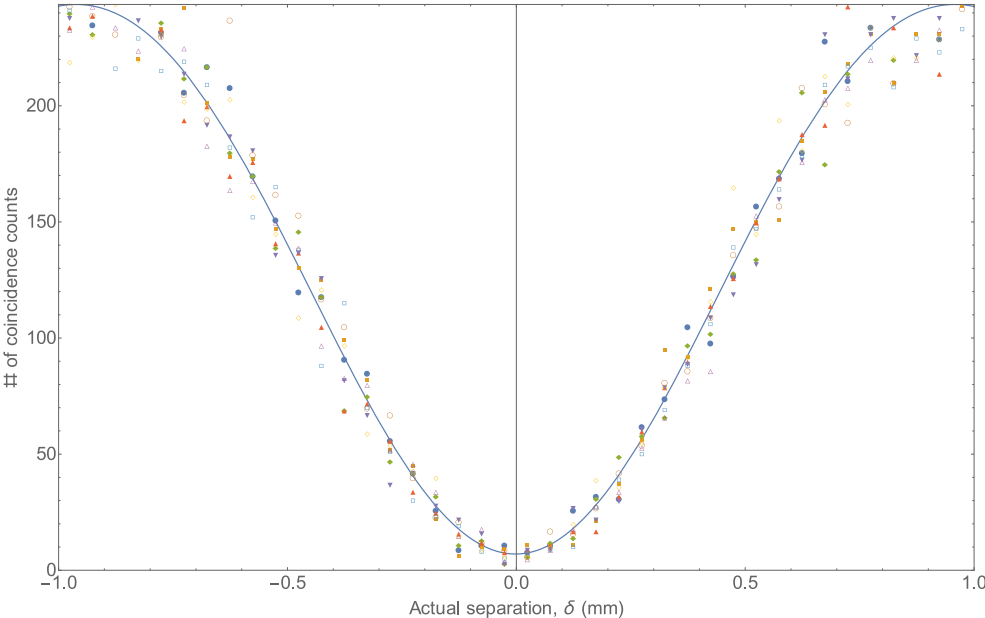


Figure 7: Raw data plot for SPLICE coarse scans. Dots are experimental photon coincidence counts plotted versus actual beam separation δ . Solid overlay is a fit to equation 2.

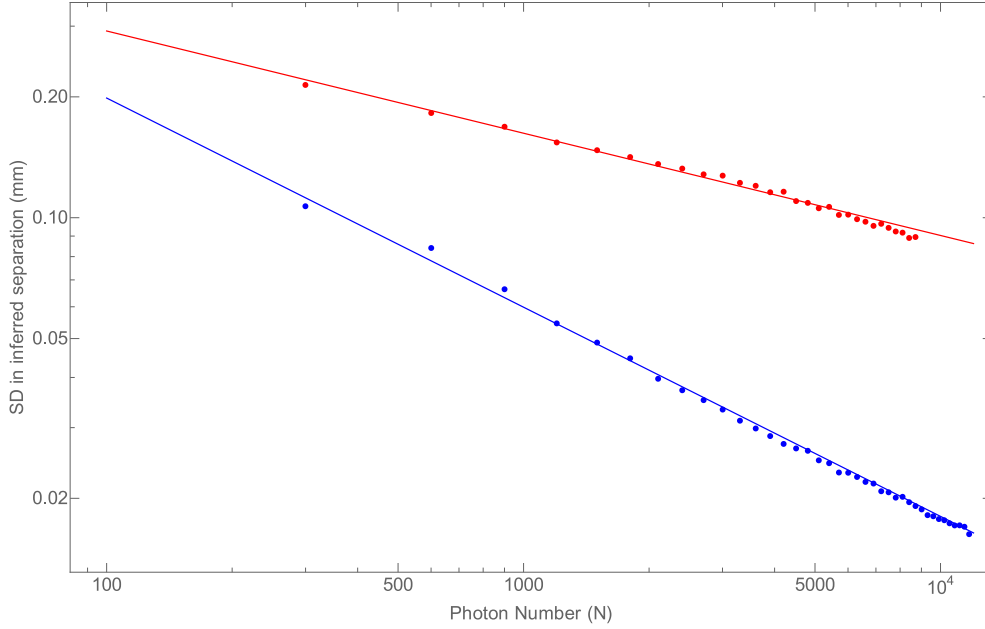


Figure 8: Monte-Carlo Scaling Analysis. Dots are the SD in inferred separation from Monte-Carlo simulations of SPLICE (blue) and IPC (red), with $\delta = 0.21\text{mm}$ averaged over 200 repetitions versus total photon number. Other parameters - i.e. σ and γ/N (see text) - were set to experimental values. The overlaid solid lines power-law fits of the form αN^β to simulation results. The fit parameters for IPC are: $\alpha = 0.943 \pm 0.031$, $\beta = -0.254 \pm 0.004$ and for SPLICE $\alpha = 2.188 \pm 0.090$, $\beta = -0.521 \pm 0.006$. While $\delta = 0.21\text{mm}$ was chosen arbitrarily for this plot, the simulation was performed for multiple values of δ . We note that with finite visibility (i.e. $\gamma \neq 0$), SPLICE also begins to scale as $N^{-1/4}$ when both δ and N are very small. It is important to note, however, that unlike IPC, this is not a fundamental scaling but is rather a result of technical limitations (i.e. imperfect visibility) in our apparatus. A scaling of $N^{-1/2}$ is retained for all δ and N when $\gamma = 0$.

Supplementary

Bias Derivation

Bias

Suppose one was tasked with estimating the value of some parameter, x , by looking at the
280 value of some random variable y , which distribution depends on x . If the expectation value of
 y equals x for *all* values of the parameter x , i.e. $\langle y \rangle_x = x$, then the random variable y is known
as an *unbiased* estimator of x . The distinction between a biased vs an unbiased estimator
is important to consider when one is trying to reason in terms of the Fisher information and
CRLB. As mentioned in the main text, a more general form of the CRLB is:

$$\sqrt{\text{Var}(y)} \geq \sqrt{\frac{1}{I_{fish}} \left(1 + \frac{\partial(\text{bias})}{\partial x} \right)}$$

285 where bias is $\langle y \rangle_x - x$. Notice that when the estimator is unbiased, this reduces to equation 4
in the main text. In the case of IPC, since the Fisher information clearly vanishes as $\delta \rightarrow 0$, an
infinite variance in the estimator δ_{est} can be avoided only if the *slope* of $\langle y \rangle_x$ tends to 0 more
quickly than I_{fish} . It is our goal in this supplementary section to demonstrate that that is indeed
the case.

Spread in estimator of δ^2

290 For IPC at small separations each image was fitted to a Taylor expansion of the detection
probability p_i (the usual sum of two Gaussians) to 2nd order:

$$p_i \approx \frac{A}{\sigma\sqrt{2\pi}} \exp\left[-\frac{x_i^2}{2\sigma^2}\right] + \frac{A\delta^2}{8\sigma^5\sqrt{2\pi}} \exp\left[-\frac{x_i^2}{2\sigma^2}\right] (x_i^2 - \sigma^2)$$

Subscripts i were added in anticipation of an image consisting of many pixels at various values
of some axis x . Performing a linear regression of a set of photon detection rates p_i yields
295 parameters A and $A\delta^2$. Notice that the design matrix, M , in this case contains only x_i 's and
 σ and so is independent of photon number N . If we now assume that the noise at each pixel

location is mutually independent, then:

$$\begin{bmatrix} \Delta A \\ \Delta (A\delta^2) \end{bmatrix} = \sqrt{\sum_j o_{ij}^2 (\Delta p_j)^2}$$

where $o_{ij} = \left[(M^T M)^{-1} M^T \right]_{ij}$. Supposing that our *only* source of noise is Poissonian in nature, then $\Delta p_j \sim \sqrt{p_j}$ so that ΔA and $\Delta (A\delta^2)$ both $\sim \sqrt{N}$.

300 Now elementary error propagation gives:

$$\Delta (\delta^2) = \sqrt{\left(\frac{\Delta (A\delta^2)}{A} \right)^2 + \left(\frac{A\delta^2}{\Delta A} \right)^2}$$

which in the small δ limit reduces to

$$\Delta (\delta^2) \approx \frac{\Delta (A\delta^2)}{A} \sim 1/\sqrt{N}$$

Thus we expect the estimate of δ^2 from this method to have a spread that scales approximately as $1/\sqrt{N}$.

“Clipping” $\delta^2 < 0$ and bias in δ

305 If there is a sufficiently large number of pixels in our image, the central limit theorem imposes a Gaussian distribution on δ^2 , with width $s = \Delta (\delta^2) = \gamma/\sqrt{N}$ where γ is some constant of proportionality. Although at first glance negative values of δ^2 appear problematic, we can avoid having to censor parts of our data where this is the case by noting that they have a natural physical interpretation if we also allow $\sigma \rightarrow -\sigma$ since the quadratic term is paired with an odd
 310 σ^5 term. We can therefore compute the moments of the distribution relevant to the mean and spread of our estimate of δ :

$$\begin{aligned} \langle \delta \rangle &= \frac{1}{s} \sqrt{\frac{2}{\pi}} \int_{-\infty}^{\infty} \sqrt{|x|} \exp \left[-\frac{(x - \delta_{actual}^2)^2}{2s^2} \right] dx \\ \langle \delta^2 \rangle &= \frac{1}{s} \sqrt{\frac{2}{\pi}} \int_{-\infty}^{\infty} |x| \exp \left[-\frac{(x - \delta_{actual}^2)^2}{2s^2} \right] dx \end{aligned}$$

In the limit where $\delta_{actual} \rightarrow 0$, we find the scalings: $\langle \delta \rangle \sim \sqrt{s} \sim N^{-1/4}$ and $\langle \delta^2 \rangle \sim s \sim N^{-1/2}$, the latter agreeing with our Monte Carlo simulations that the standard deviation or spread in

our estimate scales as $N^{-1/4}$ as well. More crucially, $\langle\delta\rangle$ can be shown to approach a constant
315 value sufficiently quickly as δ_{actual} goes to 0 for the CRLB to converge to a finite value. $\langle\delta\rangle$ is
plotted in figure 8 of the main text.

Note that the emergence of a bias in our estimate isn't specific to our treatment of the
negative tail of δ^2 ; the same bias and scalings can be obtained even if we had opted for the
lazier approach of censoring parts of our data that produce negative δ^2 values (tantamount to
320 simply "chopping" rather than "folding" that tail of the distribution). Rather, the bias is more
generally a consequence of performing the regression on δ^2 instead of δ .

The bias vanishes if the two sources have unequal intensities. The breaking of this symmetry
introduces a term in p_i that is linear in δ . If this term is much larger than the quadratic (δ^2) term,
we can use δ as a fit parameter instead, thereby obtaining an unbiased estimator. We leave the
325 analysis of this asymmetric case to a possible future work.